

Received June 28, 2019, accepted July 27, 2019, date of publication August 12, 2019, date of current version October 23, 2019.

Digital Object Identifier 10.1109/ACCESS.2019.2934582

High Resolution Lensless Terahertz Imaging and Ranging

DILYAN DAMYANOV¹, BENEDIKT FRIEDERICH¹, MILAD YAHYAPOUR^{2,3}, NICO VIEWEG², ANSELM DENINGER², KEVIN KOLPATZECK¹, XUAN LIU¹, ANDREAS CZYLWIK¹, THORSTEN SCHULTZE¹, INGOLF WILLMS¹, AND JAN C. BALZER¹

¹Chair of Communication Systems, University of Duisburg-Essen, 47057 Duisburg, Germany

²TOPTICA Photonics AG, 82166 Gräfelfing, Germany

³Institute of Microwaves and Photonics, Friedrich-Alexander University Erlangen Nürnberg, 91058 Erlangen, Germany

Corresponding author: Dilyan Damyanov (dilyan.damyanov@uni-due.de)

This work was supported in part by the German Research Council (Deutsche Forschungsgemeinschaft, DFG) in the framework of CRC/TRR196 (MARIE) for projects M05 and S01, and in part by the Open Access Publication Fund of the University of Duisburg-Essen.

ABSTRACT In this paper, we propose a fast terahertz time-domain imaging method using a radar migration algorithm. We demonstrate high-resolution imaging in reflection without any collimating or focusing optics in the terahertz beam. In the proposed method, the sample is illuminated with a divergent terahertz beam, and the receiver collects both specular and diffuse reflections. We further present calibration and post-processing methods that allow us to compensate for the inherently low signal-to-noise ratio of an unfocused terahertz beam. The feasibility of the novel imaging method is demonstrated with geometrically complex samples and a fast terahertz time-domain spectroscopy system based on electronically controlled optical sampling. We show that our concept is capable of generating images of the objects regardless of their size, shape, orientation and position relative to the transmitter and receiver antennas. Objects with edge lengths well below 400 μm can be clearly detected. The method presented here thus lends itself to arbitrary scenarios and antenna configurations.

INDEX TERMS Terahertz time-domain spectroscopy, lensless terahertz imaging, ECOPS, radar migration algorithms.

I. INTRODUCTION

Terahertz waves have a higher penetration depth than infrared waves and higher lateral resolution than microwaves, and are hence attractive for a multitude of imaging scenarios [1]. Applications demonstrated thus far include security screening [2], [3], medical research [4] and cancer screening in particular [5], non-destructive testing [6], hydration monitoring [7] and spatially resolved thickness measurements, e.g. of tablet coatings [8], [9]. In a typical imaging setup, the sample is placed at the focus of the terahertz beam, either in reflection [10] or in transmission mode [11].

Lenses or mirrors serve to collimate the terahertz beam, focus it onto the sample and guide the specular reflection from the illuminated spot to the detector. Hence, precise information about the position, orientation and shape of the sample is an *a priori* requirement for the mechanical alignment of

the optomechanics [10]–[12]. Moreover, even in the case of a “perfect” optical alignment, sharp focusing is only achieved for a very limited depth of field, and the lateral resolution still remains limited by the spot size of the terahertz beam. This becomes even more complicated since the spot size itself is usually frequency-dependent. All of these bottlenecks limit the applications of terahertz imaging in real-life scenarios, where no or only limited *a priori* information about the sample and its surface geometry is available.

In this paper, we introduce a promising imaging approach that overcomes the drawbacks of focused terahertz setups, yet maintains a high lateral and axial resolution. Our imaging scheme, adapted from classical radar techniques, uses a divergent terahertz beam without any focusing or collimating optics. A post-processing procedure compensates for the inherently lower signal-to noise ratio (SNR) of the unfocused terahertz setup. In contrast to conventional imaging systems, the lateral resolution of our approach is not limited by the spot size of the focused terahertz beam, which enables us

The associate editor coordinating the review of this manuscript and approving it for publication was Chow-Yen-Desmond Sim ¹.

to image “subwavelength”-sized objects and structures. The determining factors in our novel method are the synthetic antenna aperture and absolute bandwidth. For the evaluation and validation of the proposed method, we employ a fast terahertz time-domain spectroscopy (TDS) system based on electronically controlled optical sampling (ECOPS). With this system, we image a set of six samples of complex shape.

II. REFLECTION BASED TDS IMAGING METHOD

When a divergent beam is used for reflection-mode imaging, every section of the sample is illuminated under a different angle. If the antennas move relative to the sample, the contributions from different sections of the sample vary, and plenty of information on the sample reflectivity is obtained. In order to generate an image of the sample under test, the captured time-domain pulses are back-projected and integrated over the complete aperture. This technique is also known as migration imaging with a synthetic aperture. In this section, we first discuss the basic principle of the proposed imaging method. We use simulated broadband terahertz signals to present the advantages of a synthetic aperture for imaging, before proceeding to actual measurements in section III.

A. BASIC PRINCIPLE

The migration-based radar image reconstruction technique was first introduced by Schneider in [13] and has been successfully used and modified for different radar applications [14], [15]. In our work, the main idea of migration-based radar imaging is adapted for broadband TDS measurements. Fig. 1 illustrates the principle with an example of a single point scatterer at position (x_p, y_p) . The sample is initially illuminated with a short pulse from a transmitter positioned at $(x_{T,1}, y_{T,1})$, shown in blue in Fig. 1. The sample reflects the signal, which after a round-trip time t_1 is captured by the receiver at position $(x_{R,1}, y_{R,1})$. The detected signal $s_r(t, \mathbf{R}_n, \mathbf{T}_n)$ can be expressed as

$$s_r(t, \mathbf{R}_n, \mathbf{T}_n) = \sum_i r(\mathbf{P}_i, \mathbf{R}_n, \mathbf{T}_n) \cdot s_t(t - t_{i,n}), \quad (1)$$

where \mathbf{R}_n and \mathbf{T}_n denote the positions of the receiver and transmitter for the n -th measurement, \mathbf{P}_i is the position of the i -th point target and $r(\mathbf{P}_i, \mathbf{R}_n, \mathbf{T}_n)$ is the reflection factor describing the terahertz wave reflected from target \mathbf{P}_i onto the detector. $r(\mathbf{P}_i, \mathbf{R}_n, \mathbf{T}_n)$ is a function of the sample shape and size, the angle of incidence of the terahertz wave on the sample and the angle of incidence on the detector. $s_t(t)$ denotes the transmitted broadband terahertz signal. Assuming a constant wave propagation velocity c , the round-trip time resulting from the i -th point target and n -th measurement is

$$t_{i,n} = \frac{|\mathbf{P}_i - \mathbf{T}_n| + |\mathbf{P}_i - \mathbf{R}_n|}{c}. \quad (2)$$

In the next step, the antennas move along the x -axis, as indicated by the red transmitter-receiver pair in Fig. 1. (Note that this is a simplification to convey the general idea of the method; in the actual experiments, the antennas remain

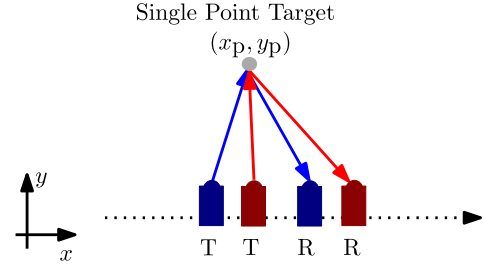


FIGURE 1. Example of a single point scatterer illuminated from different antenna positions. At the beginning the transmitter (T) and receiver (R), shown in blue, are located at $(x_{T,1}, y_{T,1})$ and $(x_{R,1}, y_{R,1})$. The antennas are then moved to new positions on the x axis, as shown in red, while the measurements continue.

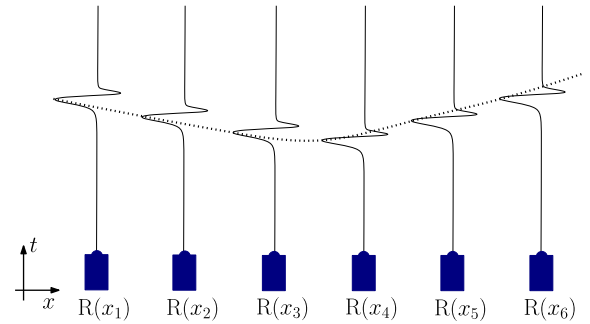


FIGURE 2. Graphical representation of the received reflection signals from a single point scatterer for 6 different positions of the receiver antenna. All reflections are located along the dotted curve.

static and the sample rotates.) Subsequent measurements therefore collect multiple reflections from the same sample, but at different antenna positions. In other words, the value of $r(\mathbf{P}_i, \mathbf{R}_n, \mathbf{T}_n)$ changes for the same sample with each antenna position. Fig. 2 shows time-domain signals captured by the receiver antenna at different positions along the x -axis. This type of data representation is also known as radargram. A radargram is a two-dimensional time-domain scan representing detected signals in time-domain as a function of the radar position. In this particular case, the peak of the received terahertz pulse represents the time-of-flight information of the measurement.

Since all reflections originate from the same single point sample, they lie on a curve (indicated by the dotted line in Fig. 2) that represents the distance from the transmitter to the sample plus the path from the sample to the receiver.

Using the time-of-flight information from the radargram and knowledge about the respective positions of receiver and transmitter antennas for each measurement, we can generate a reflectivity map $I(x_m, y_m)$ of the sample area, essentially a sum of the back-projected THz pulses

$$I(x_m, y_m) = \sum_n s_r(t - t_{m,n}, \mathbf{R}_n, \mathbf{T}_n), \quad (3)$$

where $t_{m,n} = \frac{|\mathbf{P}_m - \mathbf{T}_n| + |\mathbf{P}_m - \mathbf{R}_n|}{c}$ is the round-trip time of the pulses to and from an assumed point scatterer at \mathbf{P}_m . Eq. (3) yields a 2-dimensional matrix where every matrix element

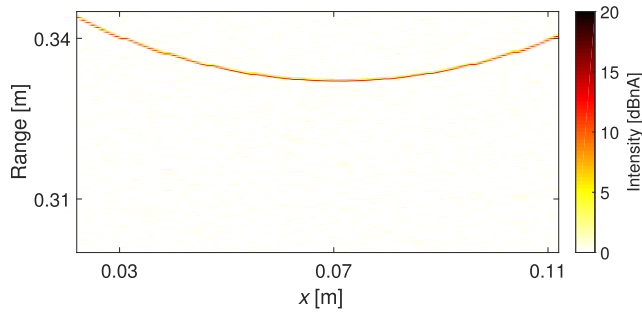


FIGURE 3. A simulated radargram resulting from a single point target at (0, 0.15) m. The horizontal axis represents the position of the receiver antenna and the vertical axis shows the distance to the reflector.

TABLE 1. Simulation parameters.

Description	Parameter
Bandwidth of the pulse	2.5 THz
Position of the point target	$x = 0$ m, $y = 0.15$ m
Initial \mathbf{T}_0	$x = -0.12$ m, $y = 0$ m
Initial \mathbf{R}_0	$x = 0.02$ m, $y = 0$ m
Step size between measurements	$\Delta x = 1$ mm
Number of measurements	$N = 101$
Imaging area	-5 mm $\leq x \leq 5$ mm, 135 mm $\leq y \leq 155$ mm

corresponds to the reflectivity coefficient of a possible single point scatterer at (x_m, y_m) . Pixels with high intensities encode the “true” image of the sample. A key advantage of this method is its simplicity, as it removes the need for any *a priori* information about the sample itself. Another characteristic attribute of this algorithm is that the image of the sample is obtained from the complete time-domain data, since the contributions of different point scatterers appear at different points in time along the pulse trace.

B. SIMULATED RESULT

Using the model described in II-A, we perform a simulation of an imaging scenario where a broadband terahertz TDS system illuminates a single point scatterer. The goal of the simulation is to assess the lateral resolution of such a measurement setup. We first consider a restricted synthetic antenna aperture for the image generation, then we use the complete radargram from the divergent broadband terahertz beam. Table 1 lists the simulation parameters. The received signals are simulated according to (1) with $r(\mathbf{P}_i, \mathbf{R}_n, \mathbf{T}_n) = 1$ for all $n = 1, \dots, N$. The resulting radargram is shown in Fig. 3. In the figure is depicted the intensity of the detected signals defined as $s_I(t, \mathbf{R}_n, \mathbf{T}_n) = 20 \log_{10} |s_r(t, \mathbf{R}_n, \mathbf{T}_n)|$ in dBnA as a function of the position of the receiver antenna and the time-of-flight. For simplicity, the time-of-flight axis is multiplied with the wave propagation speed (here the speed of light), which yields a “range” axis that directly displays the distance from the transmitter to the target and back to the receiver. We note that a single reflection is observed for each antenna position. Further, all reflections lie on a parabola similar to the graphical representation in Fig. 2.

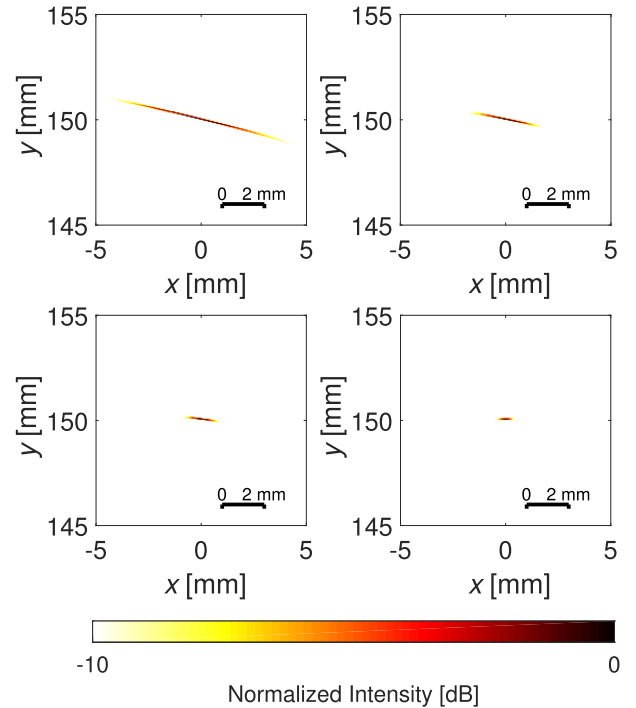


FIGURE 4. Resulting images of the simulated single point target for synthetic antenna aperture, with 10 different antenna positions (top left), 25 antenna positions (top right), 50 antenna positions (bottom left) and all antenna positions (bottom right) considered. The color coded intensity scale represents the normalized reflectivity coefficients.

Next, we generate a reflectivity map, or image, of the area under test using the back-projection of the broadband time-domain signals according to (3). Four images are generated for this simulation. Fig. 4 shows images of the area under test generated with information from 10, 25, 50 and all 101 captured pulses, respectively. The color-coded intensity scale is obtained from a logarithmic representation of the normalized reflectivity coefficients according to (3). The plots clearly demonstrates the correlation between resolution and synthetic antenna aperture. When a limited synthetic aperture is used, the resolution of the generated images degrades. Consequently, the images of the point scatterer appear blurred and distorted. Moreover, when only 10 pulses are used for the reconstruction, neither the correct position nor the size of the single point target are recovered. The number of back-projected signals is simply not sufficient to resolve a focused image. Increasing the number of back-projected pulses gradually improves the focusing capabilities of our method. Finally, the complete radargram of all 101 pulses is considered. This is equivalent to a synthetic antenna aperture with size $L_x = 140$ mm. Using the formula for classical radar migration the resolution in x-dimension is then $\delta_x \geq (\lambda_c \cdot R)/(2 \cdot L_x)$, where λ_c is the carrier wavelength and R is the distance to the sample. This results in a theoretical resolution $\delta_x \geq 150 \mu\text{m}$. The image shows a small-scale single point scatterer with a 3 dB resolution of $200 \mu\text{m}$. The simulation thus visualizes how the image resolution benefits from a large number of

measurements. This obviously comes at a cost in terms of measurement time. For a real-world application, therefore, synthetic-aperture migration imaging calls for a sufficiently fast terahertz system. One promising candidate is a terahertz TDS instrument based on ECOPS, which we will briefly describe in the next section.

III. MEASUREMENT SYSTEM AND CALIBRATION PROCEDURE

In this section, we present our measurement setup as well as a two-step calibration procedure that we apply for image post-processing.

A. MEASUREMENT SYSTEM

The measurements presented in this work are carried out with a fast terahertz TDS system (“TeraFlash smart”, TOPTICA Photonics AG, Gräfelfing, Germany), using ECOPS [16], [17]. The instrument incorporates two femtosecond lasers (“master” and “slave”) with a center wavelength of 1560 nm, a repetition rate of about 80 MHz and a pulse width below 80 fs. Whilst the “master” laser has a fixed repetition rate, that of the “slave” is variable. The pulse train of the “slave” laser is phase-locked to that of the “master”, and a slight modulation of the “slave’s” repetition rate changes the time delay between the two lasers. This concept enables a measurement speed of 1600 terahertz waveforms per second, which proves advantageous for imaging applications.

The terahertz emitter and receiver modules are photo-conductive switches (Fraunhofer Heinrich-Hertz-Institute, Berlin, Germany) [18]. Their semiconductor composition is based on an InAlAs/InGaAs heterostructure, with the emitter being iron doped [19]. Both modules are equipped with a single-mode, polarization-maintaining fiber, and are packaged in a compact housing (25 mm diameter). A silicon lens on the output side pre-collimates the emitted terahertz beam. The residual full-width half-maximum divergence angle is about 25°.

B. MEASUREMENT SETUP AND CALIBRATION PROCEDURE

For the measurements, we position the transmitter and receiver antenna in a reflection setup, as documented in the photos of Fig. 5 and Fig. 6. A fast turntable rotates the sample during the measurement. We choose the coordinate system so that the origin at (0, 0) mm coincides with the center of rotation. In all of the measurements presented in the following section, the transmitter is positioned at (−70, −150) mm and the receiver at (70, −150) mm. Fig. 5 further illustrates how the sample is illuminated with a divergent terahertz beam. Evidently, only a small amount of back-reflected energy reaches the detector, which results in a comparatively low SNR. As we will show below, a calibration of the system significantly enhances the quality of the data. The calibration consists of two steps, which are common practice in radar measurements. First, a reference signal is obtained, using a metal plate as reflector. This provides an “ideal” reflection

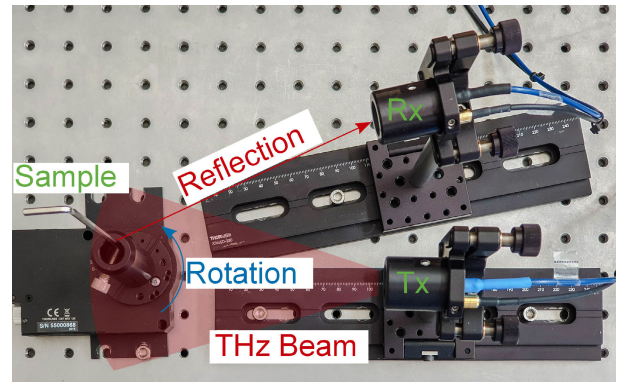


FIGURE 5. Top view of the measurement setup. The receiver and transmitter antennas are stationary while the sample is positioned on a rotation unit allowing a 360° Circular scan of the sample.

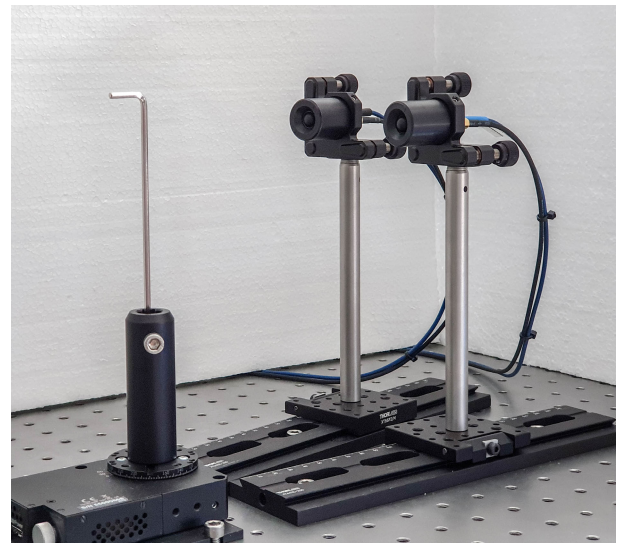


FIGURE 6. Side view of the measurement setup.

without any influence of the shape, size or material characteristics of the target. The second step involves a measurement without any sample in place, so that no terahertz signal reflected from a sample reaches the receiver. Fig. 7 shows terahertz pulses reflected from the metal plate, as measured with the unfocused setup. The single-shot trace, obtained without any averaging, shows a strong noise background. When 100 traces are averaged, the signal noise is significantly reduced. The spectrum of the averaged pulse (not shown) reaches a bandwidth of 2.5 THz with a peak dynamic range of around 30 dB. This is below the single-shot values of 3.4 THz bandwidth and 61 dB peak dynamic range obtained with off-axis paraboloids in the beam [17].

All algorithms are implemented using the programming language MATLAB® and executed using a standard personal computer with an Intel® Core™ i7-7700HQ CPU and 16 GB RAM. The processing time for the generation of a complete image is 0.6 s, which underlines the real-time capabilities of the proposed method.

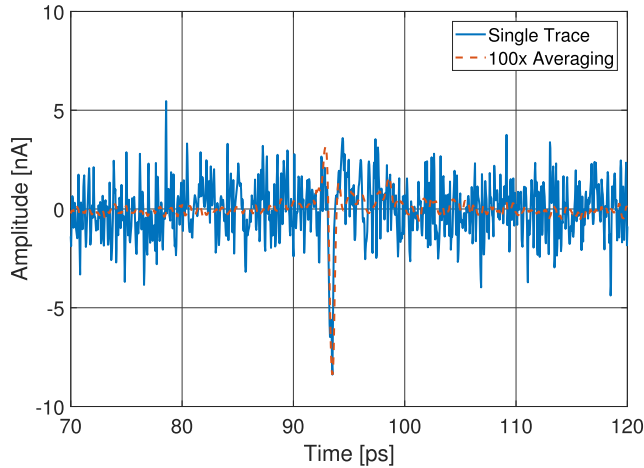


FIGURE 7. Time domain signal of a terahertz TDS measurement using a metal plate as reference target.

IV. MEASUREMENT RESULTS AND EVALUATION

The imaging method is now applied to a set of 6 test objects. We begin with the simplest geometry, a round metal post, to assess the performance of the system and the post-processing procedure. Then we analyze the resolution capabilities of the technique with 4 differently sized hex-wrenches. Finally, the method is applied to a scenario where a sample sits at an unknown position. All measurements are performed under typical indoor atmospheric conditions. We have chosen metallic objects for the initial evaluation of our method due to their high reflectivity, but we point out that the method is by no means restricted to metallic samples.

A. PROOF OF PRINCIPLE

Our first sample is a metal post with a diameter of 12.5 mm, which is mounted on the turntable. Measurements are performed continuously during a full rotation of the post. With an angular increment of 0.9° and 25 trace averages per step, the 360° rotation is completed in 14 s. The step size and the number of averages are chosen as a practical compromise between image resolution (see section II.B) and acquisition time.

To evaluate the effect of the calibration procedure, we first compute the radargram of the 360° measurement without any further post-processing. In Fig. 8, the horizontal axis corresponds to the angle of rotation, or angle of view with respect to the transmitter antenna. The vertical axis displays range information, similar to Fig. 3. The figure shows strong reflections from the metal post at a distance of approximately 275 mm. However, there are also spurious echoes further behind, which we attribute to clutter or colored noise in the time-domain trace. Evaluating the data according to equation (3) produces the image shown in Fig. 9. The shape of the metal post is clearly visible. However the image quality suffers from high noise levels and artefacts that give rise to blurred, roughly circular shapes inside and outside the reconstructed shape of the object. Next, the radargram is

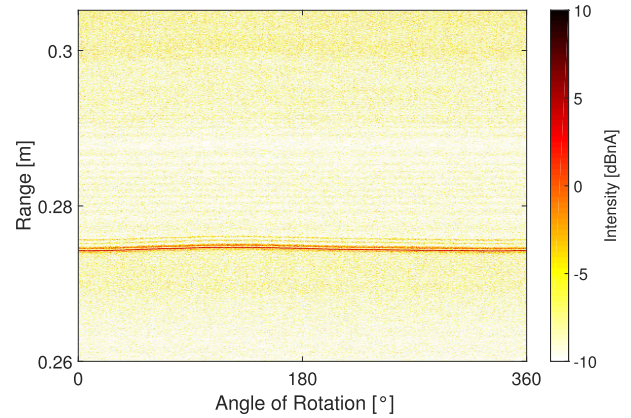


FIGURE 8. Radargram of a circular scan of a round metal post with a diameter of 12.5 mm. The horizontal axis represents the angle of rotation, the vertical axis shows the distance to the sample.

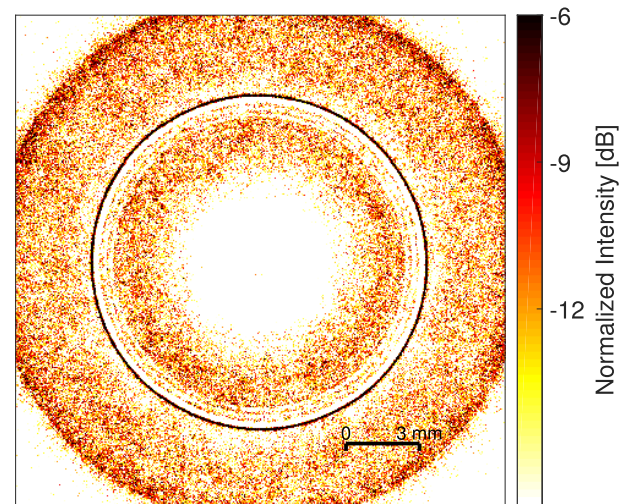


FIGURE 9. Reconstructed image of the metal post. Shape and size of the sample are correctly displayed, but the image is obscured by noise and artefacts.

post-processed (see below) and the resulting image is shown in Fig. 10. The improvement in image quality is obvious, in particular, the “halos” around the post are almost entirely suppressed.

In detail, the post-processing routine involves the following steps:

- 1 Each signal $s_r(t, \mathbf{R}_n, \mathbf{T}_n)$ is generated from 25 averaged terahertz time-domain traces.
- 2 The averaged signals are Wiener filtered according to

$$S_{r,F}(f, \mathbf{R}_n, \mathbf{T}_n) = S_r(f, \mathbf{R}_n, \mathbf{T}_n) \cdot \frac{H^*(f)}{|H(f)| + k(f)}, \quad (4)$$

where $S_r(f, \mathbf{R}_n, \mathbf{T}_n)$ is the Fourier transform of the original signal $s_r(t, \mathbf{R}_n, \mathbf{T}_n)$, $H(f)$ is the Fourier transform of the calibration measurement obtained with the metal plate, and $k(f)$ is a weighting function based on the SNR of the signal for each frequency. The values for $k(f)$ are chosen such that for higher frequencies, which contain

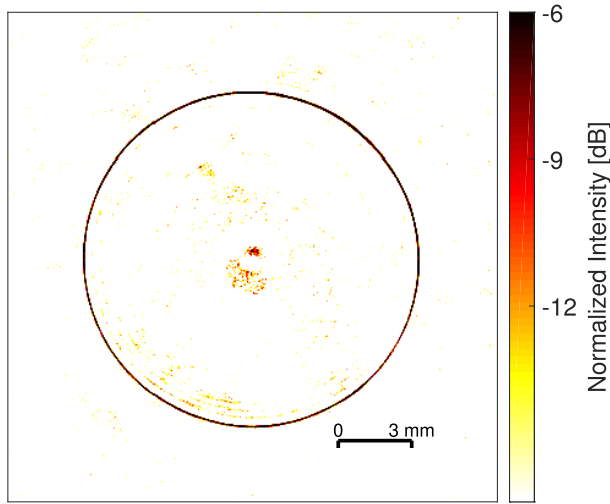


FIGURE 10. Image of the metal post after filtering. Note the improvement in image quality as compared to Fig. 9.

lower signal contribution, the Wiener filter behaves like a low-pass filter. $k(f)$ is defined as follows,

$$k(f) = \begin{cases} 1 & \text{for } f < 2.5 \text{ THz} \\ 1 - \frac{f}{20 \text{ THz}} & \text{else.} \end{cases} \quad (5)$$

- 3 The radargram is high-pass filtered with respect to the angle of view to reduce the contributions from clutter and the system noise.
- 4 Finally the image is generated according to (3), using the post-processed data.

B. EVALUATION OF RESOLUTION

To test the resolution of the imaging system as well as the precision of geometric measurements obtained from the images, we successively scan 4 hex-wrenches of different sizes: (i) 4 mm diameter and 2.3 mm edge length, (ii) 2.5 mm diameter and 1.44 mm edge length, (iii) 1.5 mm diameter and 0.86 mm edge length, and (iv) 0.75 mm diameter and 0.43 mm edge length. The images, computed by means of the algorithm presented in the previous section, are shown in Fig. 11. The images underline the strength of our approach: the shapes of each sample are clearly reproduced, with continuous contours and very low residual noise. Note that the image reconstruction does not require any input information about the shape or size of the sample. The three short diagonals (i.e. distances a, b, c between opposing sides of the hexagonal shapes as shown in Fig. 11) of each imaged object are compared with values measured with a micrometer gauge. This enables us to roughly characterize the precision of the terahertz measurement. The results, presented in table 2, show an absolute error of max. $38 \mu\text{m}$ ($< 1\%$) for 4 mm diameter. For the 2.5 mm and 1.5 mm hex-wrenches, the relative error remains on the order of 2%. An exception is the 0.75 mm sample, where an error of $40 \mu\text{m}$ ($\approx 9\%$) is observed. We surmise that this small sample may not

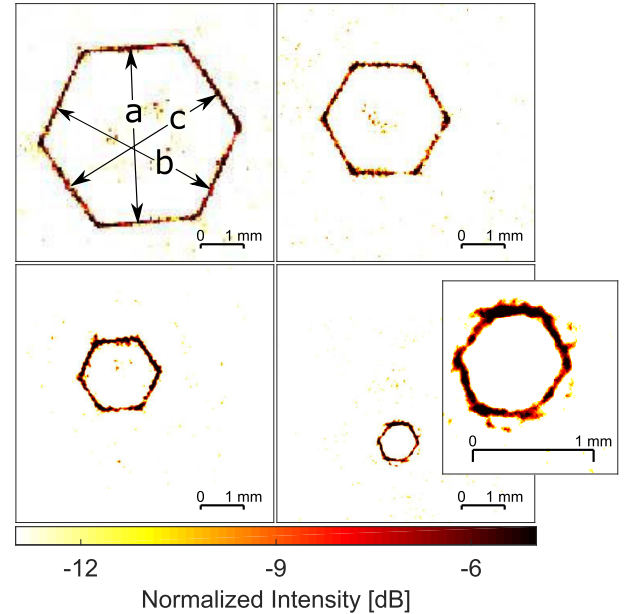


FIGURE 11. Images of hex-wrenches of different diameters: 4 mm (top left), 2.5 mm (top right), 1.5 mm (bottom left) and 750 μm (bottom right). The zoom in the last image shows the smallest hex-wrench on a larger scale. The distances a, b and c (top left) of opposing sides are used for evaluating the precision of the measurement (see Tab. 2).

TABLE 2. Precision of size measurements of the 4 hex-wrenches.

Hex-wrench measured a x b x c	Dimensions from image a x b x c	Error (Δa , Δb , Δc)
3.99 x 4.00 x 3.99 mm	4.010 x 4.035 x 4.028 mm	(20, 35, 38) μm
2.49 x 2.50 x 2.49 mm	2.527 x 2.533 x 2.496 mm	(37, 33, -6) μm
1.49 x 1.49 x 1.49 mm	1.521 x 1.485 x 1.520 mm	(31, -5, 30) μm
0.78 x 0.76 x 0.75 mm	0.820 x 0.779 x 0.741 mm	(40, 19, -9) μm

have been positioned perfectly vertical on the turntable and therefore, one side of the sample appears slightly stretched in the image. Nevertheless, the $430 \mu\text{m}$ long edges are clearly reconstructed.

C. EVALUATION FOR UNKNOWN POSITION

In all of the previous measurements, the samples were located at (0, 0) mm, i.e. at a precisely known position within the coordinate system. However, the imaging method is designed to work for samples of unknown orientation and position. In this section, we proceed to test the capabilities of the unfocused imaging system with a sample placed at different positions; only the antenna configuration remains the same. A schematic of the measurement setup is shown in Fig. 12. The sample is imaged iteratively at 6 different positions separated by 25 mm as shown in the figure. The sample, also shown in Fig. 12, consists of a metal profile with a square 7 mm base with a notch of 1 mm on each side.

For the analysis, we use no *a priori* information about the position of the sample at all. The reconstructed reflection images are presented in Fig. 13, grouped together in a single xy plane. The complex shape of the sample is correctly

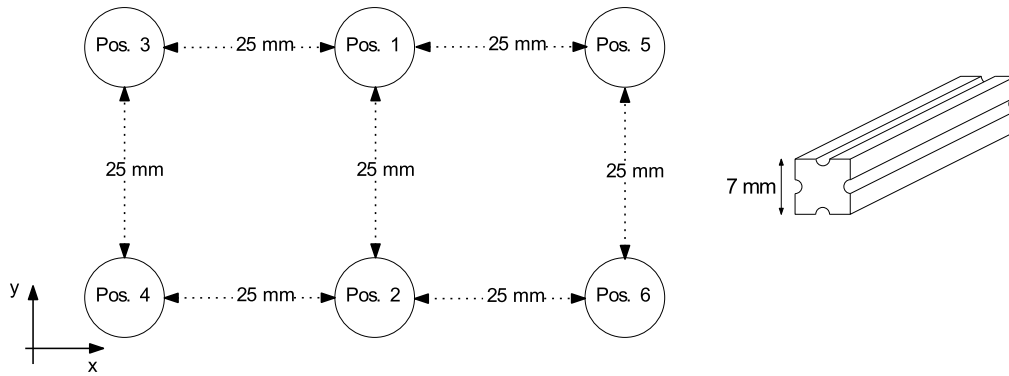


FIGURE 12. Measurement setup that mimics a sample at an unknown position. A circular scan is recorded at each of the six positions shown (left). A schematic representation of the sample used for the measurement scenario is shown on the right.

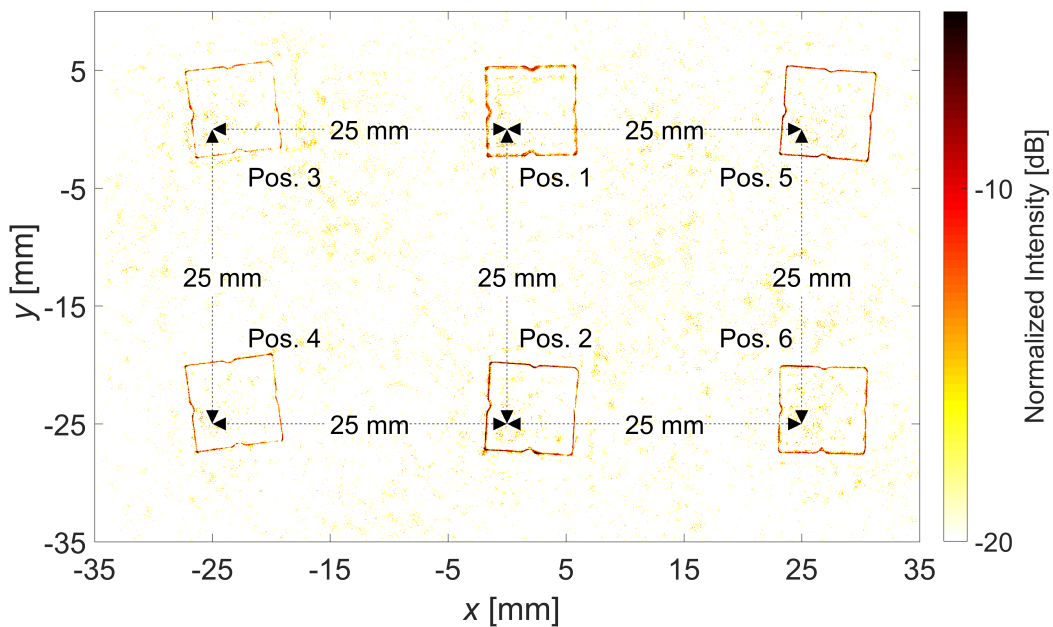


FIGURE 13. Reconstructed images, obtained with the setup of Fig. 12. The sample is scanned separately at each measurement position and then reconstructed in the same xy plane.

displayed including the notches at each side. Furthermore, the image correctly reproduces the 25 mm spacing between the individual imaging positions. This confirms that our terahertz TDS imaging method is capable of generating high-resolution images of a sample without any input information about shape, orientation and position of the object under test.

V. CONCLUSION AND OUTLOOK

In this paper, we presented a novel approach for fast broadband terahertz imaging. The measurement setup combines an ECOPS-based terahertz TDS system with state-of-the-art photoconductive antennas, and makes use of a divergent beam without any optics. The imaging method is based on a migration technique and employs careful data post-processing to suppress contributions of noise and artefacts in the image. We use a set of 6 different, geometrically complex samples to

evaluate the capabilities of the method. The results prove that the technique is able to generate high-resolution reflection images of the samples regardless of their size, shape, orientation and relative position to the transmitter and receiver antennas. The results described in section IV-C can also be interpreted as taking 6 snapshots of a continuously moving object. Therefore, under certain conditions, high-resolution images and even terahertz videos of moving objects can be envisaged. The resolution of the proposed method is based on the bandwidth and antenna aperture and not the wavelength allowing for a possible “subwavelength” image resolution.

We further demonstrate that objects with edge length as small as $400\ \mu\text{m}$ are clearly detected and correctly retrieved. The relative error of the object size, as determined from the images, is on the order of 1% for samples as small as 1.5 mm. We are confident that the new method will find practical

applications in terahertz imaging, owing to the simplicity of the experimental setup and the short time required for image acquisition.

In this work, we have limited ourselves to two-dimensional measurements of metal objects at a relatively close range. However, the distance to the objects is only limited by the SNR which depends on the opening angle of the transmitter antenna, the radar cross section of the target and the employed system. Furthermore, the proposed imaging method is not influenced by the material characteristics of the scanned object. We expect the method to be sufficiently robust even for 3D scans of an object at larger distances, and will evaluate the possibilities of three-dimensional imaging in the future.

REFERENCES

- [1] D. M. Mittleman, "Twenty years of terahertz imaging," *Opt. Express*, vol. 26, no. 8, pp. 9417–9431, Apr. 2018.
- [2] R. Appleby and H. B. Wallace, "Standoff detection of weapons and contraband in the 100 GHz to 1 THz region," *IEEE Trans. Antennas Propag.*, vol. 55, no. 11, pp. 2944–2956, Nov. 2007.
- [3] J. Gao, Z. Cui, B. Cheng, Y. Qin, X. Deng, B. Deng, X. Li, and H. Wang, "Fast three-dimensional image reconstruction of a standoff screening system in the terahertz regime," *IEEE Trans. THz Sci. Technol.*, vol. 8, no. 1, pp. 38–51, Jan. 2018.
- [4] K. Humphreys, "Medical applications of terahertz imaging: A review of current technology and potential applications in biomedical engineering," in *Proc. 26th Annu. Int. Conf. IEEE Eng. Med. Biol. Soc.*, San Francisco, CA, USA, Sep. 2004, pp. 1302–1305.
- [5] S. Nakajima, H. Hoshina, M. Yamashita, C. Otani, and N. Miyoshi, "Terahertz imaging diagnostics of cancer tissues with a chemometrics technique," *Appl. Phys. Lett.*, vol. 90, no. 4, 2007, Art. no. 041102.
- [6] M. Scheller, S. F. Dürschmidt, M. Stecher, and M. Koch, "Terahertz quasi-time-domain spectroscopy imaging," *Appl. Opt.*, vol. 50, no. 13, pp. 1884–1888, May 2011.
- [7] R. Gente, A. Rehn, T. Probst, E.-M. Stübling, E. C. Camus, A. A. Covarrubias, J. C. Balzer, and M. Koch, "Outdoor measurements of leaf water content using THz quasi time-domain spectroscopy," *J. Infr., Millim., THz Waves*, vol. 39, no. 10, pp. 943–948, Oct. 2018.
- [8] J. A. Zeitler and Y.-C. Shen, "Industrial applications of terahertz imaging," in *Terahertz Spectroscopy and Imaging* (Springer Series in Optical Sciences), vol. 171, K. Peiponen, A. Zeitler, M. Kuwata-Gonokami, Eds. Berlin, Germany: Springer, 2012, ch. 18, pp. 451–489.
- [9] S. Zhong, Y.-C. Shen, M. Evans, J. A. Zeitler, R. K. May, L. F. Gladden, and C. Byers, "Quantification of thin-film coating thickness of pharmaceutical tablets using wavelet analysis of terahertz pulsed imaging data," in *Proc. 34th Int. Conf. Infr., Millim., THz Waves*, Busan, South Korea, Sep. 2009, pp. 1–2.
- [10] E. Stübling, A. Rehn, T. Siebrecht, Y. Bauckhage, L. Öhrström, P. Eppenberger, J. C. Balzer, F. Rühli, and M. Koch, "Application of a robotic THz imaging system for sub-surface analysis of ancient human remains," *Sci. Rep.*, vol. 9, Mar. 2019, Art. no. 3390.
- [11] Z. Song, S. Yan, Z. Zang, Y. Fu, D. Wei, H.-L. Cui, and P. Lai, "Temporal and spatial variability of water status in plant leaves by terahertz imaging," *IEEE Trans. THz Sci. Technol.*, vol. 8, no. 5, pp. 520–527, Sep. 2018.
- [12] E. Stübling, Y. Bauckhage, E. Jelli, B. Fischer, B. Globisch, M. Schell, A. Heinrich, J. C. Balzer, and M. Koch, "A THz tomography system for arbitrarily shaped samples," *J. Infr., Millim., THz Waves*, vol. 38, no. 10, pp. 1179–1182, Oct. 2017.
- [13] W. A. Schneider, "Developments in seismic data processing and analysis (1968–1970)," *Geophysics*, vol. 36, no. 6, pp. 1043–1073, Dec. 1971.
- [14] X. Zhuge, A. G. Yarovoy, T. Savelyev, and L. Ligthart, "Modified Kirchhoff migration for UWB MIMO array-based radar imaging," *IEEE Trans. Geosci. Remote Sens.*, vol. 48, no. 6, pp. 2692–2703, Jun. 2010.
- [15] T. Sakamoto, T. Sato, P. J. Aubry, and A. G. Yarovoy, "Ultra-wideband radar imaging using a hybrid of Kirchhoff migration and Stolt F-K migration with an inverse boundary scattering transform," *IEEE Trans. Antennas Propag.*, vol. 63, no. 8, pp. 3502–3512, Aug. 2015.
- [16] R. J. B. Dietz, N. Vieweg, T. Puppe, A. Zach, B. Globisch, T. Göbel, P. Leisching, and M. Schell, "All fiber-coupled THz-TDS system with kHz measurement rate based on electronically controlled optical sampling," *Appl. Sci.*, vol. 39, no. 22, pp. 6482–6485, Nov. 2014.
- [17] M. Yahyapour, A. Jahn, K. Dutzi, T. Puppe, P. Leisching, B. Schmauss, N. Vieweg, and A. Deninger, "Fastest thickness measurements with a terahertz time-domain system based on electronically controlled optical sampling," *Appl. Sci.*, vol. 9, no. 7, Mar. 2019, Art. no. 1283.
- [18] R. J. B. Dietz, B. Globisch, M. Gerhard, A. Velauthapillai, D. Stanze, H. Vieweg, and M. Koch, T. Göbel, and M. Schell, "64 μ W pulsed terahertz emission from growth optimized InGaAs/InAlAs heterostructures with separated photoconductive and trapping regions," *Appl. Phys. Lett.*, vol. 103, no. 6, Jul. 2013, Art. no. 061103.
- [19] B. Globisch, R. J. B. Dietz, R. B. Kohlhaas, T. Göbel, M. Schell, D. Alcer, M. Semtsiv, and W. T. Masselink, "Iron doped InGaAs: Competitive THz emitters and detectors fabricated from the same photoconductor," *J. Appl. Phys.*, vol. 121, no. 5, Jan. 2017, Art. no. 053102.



DILYAN DAMYANOV received the master's degree in communication engineering from the University of Duisburg-Essen, Germany, in 2014, where he is currently pursuing the Ph.D. degree in electrical engineering.

Since 2014, he has been a Research Assistant with the Chair of Communication Systems, University of Duisburg-Essen. His current research interest includes broadband radar sensors for fire and security applications and especially radar localization, wavefront detection, and imaging techniques. Since 2016, he has been a part of the MARIE project for mobile material characterization and localization by electromagnetic sensing using mobile THz systems.



BENEDIKT FRIEDERICH received the M.Sc. degree in electrical engineering from the University of Duisburg-Essen, Germany, in 2013, where he is currently pursuing the Ph.D. degree in electrical engineering.

Since 2013, he has been a Research Assistant with the Chair of Communication Systems, University Duisburg-Essen. His current research interest includes the digital signal processing for radar applications in terms of synthetic aperture for fire and security applications and especially, joint imaging and material characterization techniques. Since 2016, he has been a Fellow of the MARIE project for mobile material characterization and localization by electromagnetic sensing using mobile THz systems.



MILAD YAHYAPOUR received the M.Sc. degree in advanced optical technologies from the Friedrich-Alexander-Universität Erlangen-Nürnberg, in 2013. He is currently pursuing the Ph.D. degree in collaboration with TOP-TICA Photonics and the Friedrich-Alexander-Universität Erlangen-Nürnberg. He joined the Terahertz Group, TOPTICA Photonics, in 2013. His dissertation focuses on the development and characterization of a fast terahertz time-domain systems. He is currently a Research and Development Engineer with TOPTICA Photonics.



the terahertz properties of liquid crystals.

NICO VIEWEG was born in Ueckermünde, Germany, in 1976. He received the Ph.D. degree in electrical engineering from the Technical University of Braunschweig, in 2011, where he involved in the terahertz properties of liquid crystals. In 2012, he joined TOPTICA Photonics AG, where he serves as the Director of the Terahertz Research and Development Team. He has authored or coauthored more than 30 publications on terahertz science and technology, including a book chapter on



He has authored or coauthored more than 20 publications on terahertz instrumentation and applications, including a book chapter on photomixing.

ANSELM DENINGER born in Frankfurt in 1972. He received the degree in physics from the University of Mainz, Germany, and the Diploma and Ph.D. degrees having investigated the use of spin-polarized helium-3 gas for magnetic-resonance imaging of human lungs and airways, in 1997 and 2000, respectively. He received the First Prize from the Behnken-Berger Foundation for his Ph.D. thesis, in 2002.

In 2001, he joined TOPTICA Photonics, where he involved in laser stabilization techniques and contributed to building TOPTICA's first commercial terahertz systems. In 2006, he was appointed as a Product Manager, where his responsibilities include time-domain and frequency-domain terahertz technologies.



material characterization and imaging.

KEVIN KOLPATZECK received the B.S. and M.S. degrees in electrical engineering and information technology from the University of Duisburg-Essen, Germany, in 2013 and 2016, respectively, where he is currently pursuing the Ph.D. degree in electrical engineering and information technology with the Chair of Communication Systems (NTS).

His current research interests include terahertz photonics, beamforming at terahertz frequencies, and applications of terahertz technology in material

Mr. Kolpatzeck has been an UDE Scholar, from 2011 to 2016. He was a recipient of the Rohde and Schwarz Best Bachelor Award, in 2014, and the VDE Rhein-Ruhr Award for Excellent Graduations, in 2016.



XUAN LIU received the B.S. degree in electrical and electronic engineering and the M.S. degree in communications engineering from the University of Duisburg-Essen, in 2015 and 2017, respectively. She is currently pursuing the Ph.D. degree in electrical engineering and information technology with the Department of Communication Systems (NTS), University of Duisburg-Essen, Germany.

Her current research interests include the development and investigation of dielectric THz passive components, and the study of beamforming concepts for THz frequencies.



heading the Research Group of Microcellular Radio Systems. Since 2002, he has been the Head of the Chair of Communication Systems, University of Duisburg-Essen.

His current research interest includes radio communications on link and system level with special focus on adaptive multicarrier MIMO techniques. His several research activities focus on utilizing high frequency (up to THz) electromagnetic waves with applications in the field of extreme wideband communications and radar systems. He is also interested in the application of radio communications in the field of technical security systems. Since 2014, he has been the Chairman of the European Society for Automatic Alarm Systems (EUSAS).



THORSTEN SCHULTZE received the Diploma degree in electrical engineering from the University of Duisburg-Essen, in 2003, and the Ph.D. degree in electrical engineering, in 2010.

He is currently an Academic Senior Councilor (Akademischer Oberrat) with the Chair of Communication Systems, University of Duisburg-Essen. His current research interests include automatic fire detection technologies and broadband microwave, and THz analyses for fire and security applications.



with the University of Duisburg-Essen, as a Senior Professor.

His current research interests include automatic fire detection technologies and especially, broadband THz radar sensors for fire detection and fire-fighting applications. Since 1996, he has been a member of the executive committee of the European Society for Automatic Alarm Systems (EUSAS). In 2018, he received the EUSAS Honorary Membership. As a coauthor, he received the Best Student Paper Award at the IEEE ICUBW 2011 Conference and the Best Paper Award at the IEEE ICUBW 2014 Conference.



JAN C. BALZER was born in Unna, Germany, in 1984. He received the Dipl.-Ing. degree (FH) in telecommunications from the University of Applied Science Dortmund, Germany, in 2008, and the M.Sc. degree in electrical engineering and information technology and the Ph.D. degree in electrical engineering (involved in ultrafast semiconductor lasers) from the Ruhr-University Bochum, Germany, in 2010 and 2014, respectively.

In 2015, he joined as a Postdoctoral Research Fellow with the Group of Prof. Martin Koch, Philipp-University Marburg. Since 2017, he has been an Assistant Professor with the Faculty of Engineering, University of Duisburg-Essen, where he combines his knowledge of ultrafast semiconductor lasers with his expertise in system building of THz spectrometers. His current research interest includes THz technology and its application.

...

DuEPublico

Duisburg-Essen Publications online

UNIVERSITÄT
DUISBURG
ESSEN

Offen im Denken

ub

universitäts
bibliothek

This text is made available via DuEPublico, the institutional repository of the University of Duisburg-Essen. This version may eventually differ from another version distributed by a commercial publisher.

DOI: 10.1109/ACCESS.2019.2934582

URN: urn:nbn:de:hbz:464-20191128-120957-2



This work may be used under a Creative Commons Attribution 4.0 License (CC BY 4.0) .